Milled nanodiamonds overproduce solvated electrons while scavenging hydroxyl radicals under gamma irradiation

Florent Ducrozet, Emilie Brun, Hugues Girard, Jean-Charles Arnault, Cécile Sicard-Roselli

Milled Nanodiamonds Overproduce Solvated Electrons while Scavenging Hydroxyl Radicals under Gamma Irradiation

Florent Ducrozet[1,2], Emilie Brun[1], Hugues A. Girard[2], Jean-Charles Arnault[2] and Cécile Sicard-Roselli[1,].*

1. Institut de Chimie Physique, UMR 8000, CNRS, Université Paris-Saclay, 91405 Orsay Cedex, France

2. Université Paris-Saclay, CEA, CNRS, NIMBE, 91191 Gif sur Yvette, France

Corresponding author: cecile.sicard@universite-paris-saclay.fr

Keywords: nanodiamonds, HPHT milling, irradiation, solvated electrons, hydroxyl radicals

Abstract

Among the different nanodiamonds, milled nanodiamonds (MNDs) from high pressure high temperature (HPHT) synthesis exhibit a crystalline quality close to the bulk diamond, making it a serious candidate for quantum or energy-related fields. In this study, MNDs aqueous suspensions with oxidized (MND-Ox) and hydrogenated (MND-H) surface chemistries were irradiated with gamma-rays. Using optimized nanoparticle-compatible methods, we revealed that MNDs in suspension enhance the production of solvated electrons under irradiation, with a higher yield for MND-H. Also, for the first time, a surface chemistry-dependent scavenging effect of hydroxyl radicals was highlighted for this type of nanodiamonds.

Introduction

Among all carbon nanostructures, nanodiamonds (NDs) exhibit promising properties for biomedical and energy-related applications[1] as their thermal[2], electrical[3], and hardness[4] hallmarks

come along with chemical stability[5] and biocompatibility[6]. The major route for high-scale production of NDs is detonation of carbon-containing explosives, leading to quasi-monodisperse particles around 5 nm with a defectuous crystalline core. However, over the last five decades, mechanical milling has evolved from a standard technique in metallurgy to a novel synthetic route for a wide variety of materials including nanocrystalline or nanocomposite ones[7]. To date, it is also one of the main methods to obtain commercial NDs, by milling of natural or synthetic diamond, the latter being obtained by high pressure high temperature (HPHT) or chemical vapor deposition (CVD) growth. Milled NDs (MNDs), commercially available with the smallest average particle size around 20 nm, even if more polydisperse than detonation nanodiamonds (DNDs), present a better crystallinity, closer to bulk diamond, and exhibit clear crystallographic facets[8]. That's why till now they garnered researchers' interest for very specific uses such as highly stable fluorescent biomarkers[9], magnetic sensors[10] or single photon emitters for quantum information processing[11].

To envision new applications to MNDs, in nanomedicine or energy-related fields for example, it is of interest to investigate their behavior towards radical species, such as hydroxyl radicals ($HO^{\bullet}$) or solvated electrons (e^-_{solv}). In fact, MNDs[12] (from natural source) or DNDs[13] are able to enhance the production of solvated electrons into water under UV or visible illumination when their surface is hydrogenated. In previous work, higher energy photons were used to irradiate DNDs aqueous suspensions and in the presence of hydrogenated DNDs, but not oxidized, hydroxyl radicals and solvated electrons were available in solution in equivalent and higher amounts than in water only[14]. This leads us to study how MNDs react under gamma irradiation, depending on their surface chemistry.

Experimental Section

Materials

Milled nanodiamonds (MNDs) were purchased from Van Moppes (SYP 0-0.05, purity > 99,9%). The polydispersity of the powder was assessed by particle size measurement on cryo-electronic microscopy observations (Figure S1).

Coumarin (purity > 99%), 7-hydroxycoumarin (7-OHCou, purity 99%) and 2,3-diaminonaphthalene (2,3-DAN, purity > 95%) were purchased from Sigma Aldrich. Sodium nitrate and sodium nitrite (purity 98.5%) were purchased from Acros Organics.

2,3-DAN aqueous solution was prepared in 0.63 N HCl with 0.16 mM final concentration.

All aqueous solutions and dilutions were made with ultra-pure water (18.2 MΩ.cm) and kept refrigerated between experiments.

Modifications of nanodiamond surface and aqueous suspension preparation

Oxidized MNDs (MND-Ox) were obtained by annealing as-received particles for 4h30 at 410°C under atmospheric pressure of air. Hydrogenated MNDs (MND-H) were obtained by annealing MND-Ox under H_2 (50 SCCM, atmospheric pressure) for 5h, at 750°C. All the annealing treatments were performed using a Carbolite Gero tubular furnace.

Aqueous NDs suspension preparation

Annealed powders were collected in a 15 mL plastic tube and the volume was completed to 4 mL with ultrapure water. Powder dispersion was obtained by a sonication step of 30 min with a 1 s on/off period and an amplitude of 60% (Cup Horn Bioblock Scientific 750 W, equipped with a cooling system with a programmed temperature of 10°C). Finally, MNDs suspensions were collected after centrifugation at 2400 g for 40 minutes, to isolate the dispersed MNDs from the aggregates/agglomerates.

X-Ray Diffraction analysis (XRD)

Crystalline structure and average sizes of nanodiamonds were identified using a D2-Phaser diffractometer (Bruker) equipped with a CuKα X-rays source. The recorded range of 2Θ angles was 10° to 100°. Analyses were realized on *ca*. 10 mg of powder deposited onto a silicon substrate. Diffractogram of the substrate alone was subtracted from the sample's signal. FWHM measurement and subsequent crystallite size determination was realized on the diamond (111) diffraction peak at 44°.

Specific surface area measurements

The specific surface area was determined by N_2 adsorption using the single point B.E.T. (Brunauer, Emmett and Teller) approach and a 3Flex instrument (Micromeretics, France). 20 to 60 mg of MNDs were degassed under vacuum for 6h at 180°C (VacPrep06, Micromeretics) for removal of impurities and then analysis was realized under N_2 at -196°C.

Size determination by microscopy

Diameters distribution of MNDs particles was realized by manual analysis of cryo-EM observations (Figure S1). Microscopy equipment and observation parameters were already described in a previous study[15]. The statistics were realized on 300 particles.

Fourier Transform Infrared (FTIR) measurements

Infrared spectra were recorded with a Bruker Vertex 70 spectrometer equipped with a diamond ATR system (MIRacle, PIKE Technologies). 2 µL of MNDs suspension in water were deposited and dried on the ATR crystal before analysis. The acquisition represents the average of 128 scans recorded with a 4 cm^{-1} resolution at room temperature and ambient atmosphere with a nitrogen-

cooled MCT detector. A break was applied in the 2240–2400 cm^{-1} region to avoid the contribution of atmospheric CO_2 absorption bands.

X-Ray Photoelectron Spectroscopy (XPS)

10 µL of MNDs suspension were deposited on a silicon substrate covered by a gold coating made by evaporation to limit the charge phenomenon during analysis. The substrates were dried at ambient temperature and pressure before analysis. XPS measurements were performed on a Kratos Analytical Axis Ultra DLD spectrometer equipped with a monochromated Al Kα (1486.6 eV) X-ray source and a charge compensation system (Manchester, UK). The take-off angle was set at 90° relative to the sample surface. Spectra were acquired at a pass energy of 160 eV for the survey and 40 eV for core levels (O_{1s}, C_{1s}). C_{1s} spectra shown in this study were acquired at 10 eV to reach a higher energy resolution. Binding energies were referenced to the $Au_{4f7/2}$ peak located at 84 eV. After the background subtraction by a Shirley correction, a curve fitting procedure was carried out to extract the components of the C_{1s} core level using Voigt functions with a Lorentzian to Gaussian ratio of 30% (Figure S2).

Dynamic Light Scattering (DLS) and zeta potential measurements

Hydrodynamic diameters and zeta potentials (ZP) were measured by a Malvern NanoZS in DTS1061 cells. Acquisitions were realized on 0.5 $mg.mL^{-1}$ suspensions at 25°C with a 173° backscattered angle. For size measurements, a refractive index of 2.417 was used. For ZP measurements, 150 V was applied (Smoluchowski equation). Both sizes and ZP results are the average of 30 independent measurements.

Irradiation of nanodiamonds aqueous suspensions

Irradiation experiments were performed using a panoramic ^{60}Co source (IL60PL Cis-Bio International, photons of 1.17 and 1.33 MeV) with dose rates between 0.5 and 1.5 $Gy.min^{-1}$ depending on the chosen distance from the gamma source. Dosimetry was determined using a Fricke dosimeter[16]. For each MNDs concentration, independent samples were irradiated at different doses between 0 and 8 Gy. Gamma irradiation of water leads to the formation of radical and molecular species, among which hydroxyl radicals and solvated electrons (Eq. 1).

$$H_2O \xrightarrow{\gamma} e^-_{solv}, HO^\bullet, H_3O^+, H^\bullet, H_2, H_2O_2 \quad (1)$$

For ^{60}Co disintegration, the formation yields of $HO^\bullet$ and e^-_{solv} are 0.28 $\mu mol.J^{-1}$ at neutral pH.

For irradiation experiments, coumarin or sodium nitrate solutions were added to MNDs suspensions. Their respective final concentrations were comprised between 0.2 and 1.5 mM for coumarin or equal to 2 mM for sodium nitrate.

After irradiation of MNDs suspension in the presence of coumarin or nitrate ions, NaCl (1% w/v final) was added to each sample to induce aggregation and samples were centrifuged (20000 g, 5 min) to remove MNDs and collect the supernatant for further analysis. Two different aqueous suspensions of MND-H were used in this study.

Quantification of hydroxyl radicals

Quantification of hydroxyl radicals was realized using coumarin as a probe. $HO^\bullet$ can add to several positions of coumarin rings and among the hydroxylated products, 7-hydroxycoumarin (7-OH Cou) is fluorescent[17]. 7-OH Cou formed during irradiation was quantified by spectrofluorometry with a microplate reader (Synergy H1 microplate reader, Biotek, excitation 326 nm, emission 450 nm). Calibration curves were made with commercial 7-OHCou in the presence of coumarin at the same concentration as in the irradiation experiments to take into account the intern filter effect[18].

Quantification of solvated electrons

Post-irradiation, supernatants were mixed with 2,3-DAN solution in a (2:1) v/v ratio. After incubation for 10 min in the dark at room temperature, NaOH solution (final concentration 0.44 M) was added. Fluorescence was detected with excitation at 360 nm and emission at 403 nm. Calibration curves were made using the same protocol with sodium nitrite solutions.

High-Performance Liquid Chromatography (HPLC)

Coumarin and hydroxycoumarins were analyzed by HPLC (HP 1100 Series, Agilent) and hydrophobic separation was performed on a C18 column (25 cm length, 4.6 mm intern diameter). 100 µL of supernatants were injected. Mobile phases were A: (89 % water, 10 % methanol and 1 % acetic acid) and B: (89 % methanol, 10% water and 1% acetic acid). Gradient elution was 0 % B during 5 min, 0-30 % B in 5 min, 30-50 % B in 20 min and 50-100 % B in 5 min, with a flow rate of 0.8 $mL.min^{-1}$. Chromatograms were plotted with absorbance detection at 280 nm. Peaks were attributed as labeled by comparison to standard hydroxycoumarins injected under the same chromatographic conditions. Chromatograms were realigned to 6-hydroxycoumarin peak and baseline corrections were applied when necessary.

Results

This work aims to quantify solvated electrons and hydroxyl radicals available in solution when MNDs aqueous suspensions were submitted to ionizing radiation. As surface chemistry was shown to play a decisive role for other NDs[19], we decided to focus on hydrogenated (MND-H) and oxidized (MND-Ox) MNDs. Starting from a commercial powder, we analyzed the particles before and after treatments to obtain an exhaustive characterization of our samples.

Characterization of nanodiamonds

First, the commercial powder was analyzed by XRD, N_2 adsorption and microscopy to confirm the crystalline structure and obtain the specific surface area of untreated (as-received) MNDs. Results are presented in Figure 1.

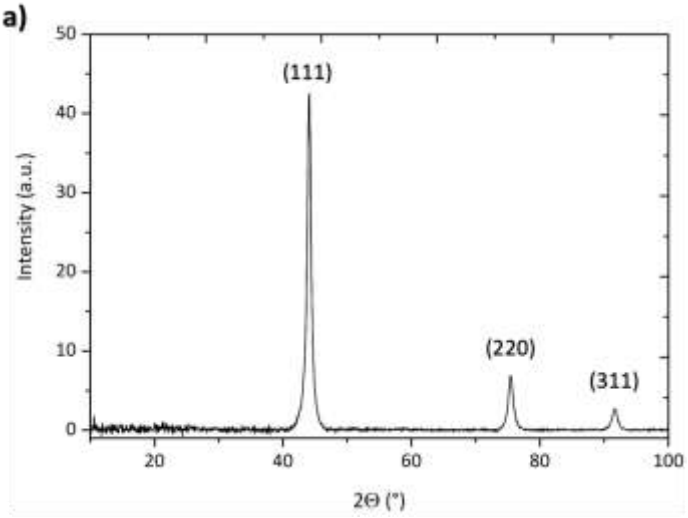

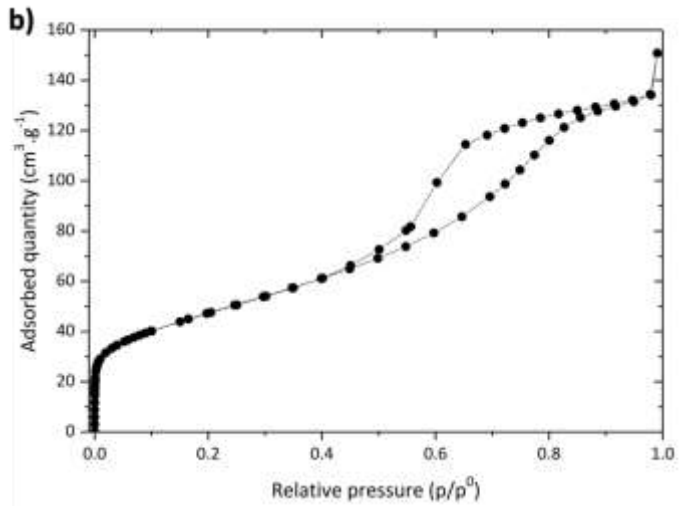

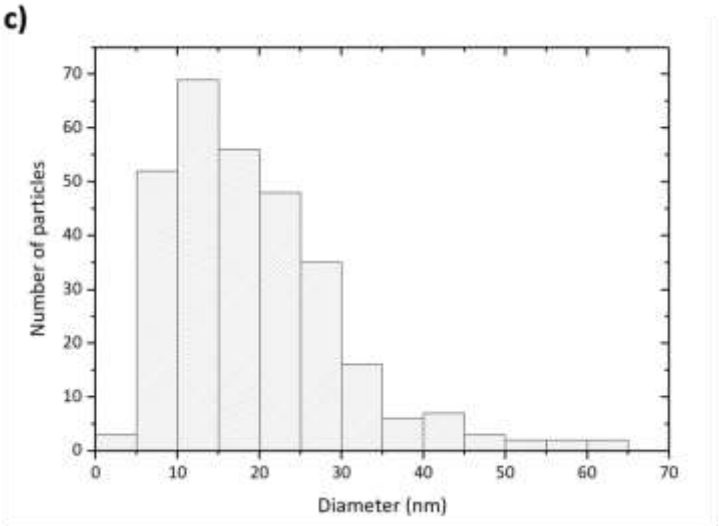

Figure 1: Characterization of untreated MNDs powder. a) XRD diffraction pattern, b) N_2 adsorption-desorption isotherm and c) Size distributions of untreated MNDs obtained by analysis of cryo-EM images

The diffraction pattern of as-received MNDs particles revealed the presence of three different peaks associated with (111), (220) and (311) cubic diamond planes at respectively $2\Theta = 44°$, 75.4° and 91.6°. The analysis of the (111) diffraction peak (FWHM) allowed the determination of the average size of the crystalline core, which was *ca*. 12 nm. No signal was detected at $2\Theta \approx 25°$ corresponding to (002) graphite planes, confirming that these particles have a negligible content of sp^2-organized carbon at their surface[20]. Figure 1b depicts the N_2 adsorption-desorption isotherm of untreated MNDs. A type IV hysteresis isotherm can be observed, corresponding to mesoporous materials[21] with pores of 2-50 nm[3]. B.E.T. calculations allowed the determination of an average specific surface area of 170 $m^2.g^{-1}$ which supports other values from the literature[22]. Considering a spherical geometry for MNDs, the corresponding diameter would be *ca*. 10 nm which is in close agreement with XRD results. In addition, the diameter distribution was also evaluated by cryo-electronic microscopy. According to manual measurements on 300 particles, the mean diameter was 19 ± 10 nm, and the median was 17 nm. This size is slightly higher than the one estimated by

XRD and N_2 adsorption, but since the observations used for this distribution were made without high resolution, the smallest particles may not be detected, leading to an overestimation of the mean diameter.

A post-treatment is necessary for the homogenization of the MNDs' surface chemistry. Oxidation and subsequent hydrogenation treatments were performed on MNDs by annealing under air and H_2, leading to MND-Ox and MND-H, respectively. A temperature of 750°C was chosen for thermal hydrogenation to ensure an optimized reduction of oxidized functions[15]. These thermal treatments did not significantly affect the specific surface area of the powders as verified with N_2 adsorption experiments (Figure S3). Annealed powders were then dispersed in ultrapure water by sonication and centrifugation steps. MND-Ox and MND-H suspensions were characterized by FTIR, DLS, zetametry (Figure 2) and XPS (Table 1).

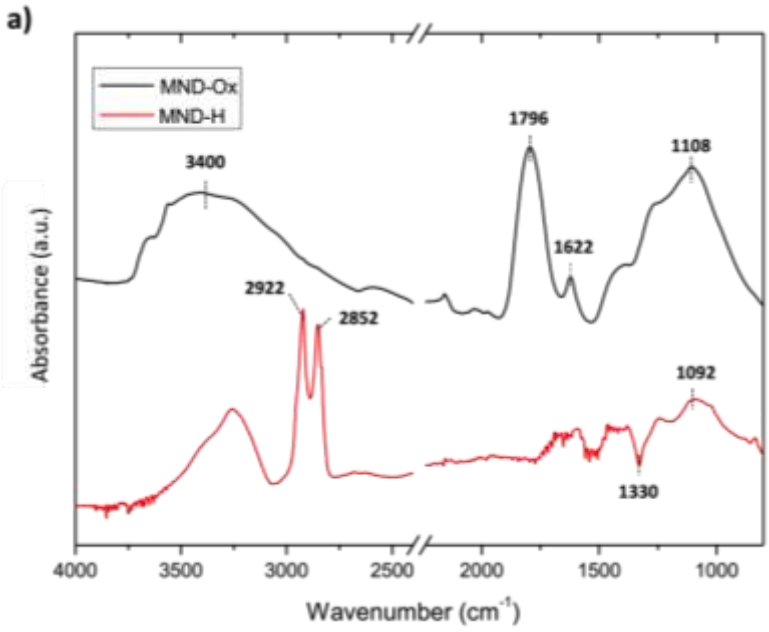

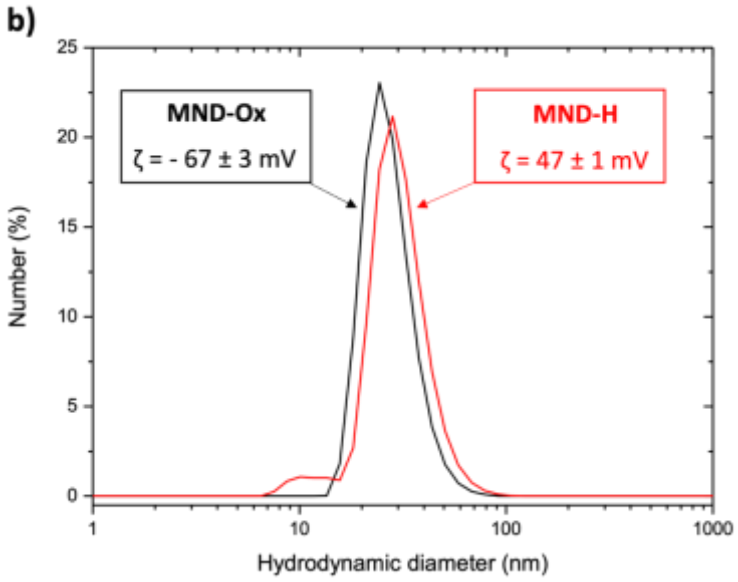

Figure 2 : Characterization of MND-H and MND-Ox suspensions in water. a) FTIR spectra obtained on dried suspensions, b) Hydrodynamic diameter distribution (in number) obtained from DLS analysis for MNDs particles. Associated zeta potentials are presented in each insert.

Fourier Transform Infrared (FTIR) spectroscopy is a reference method for the characterization of NDs' surface chemistry[23]. The spectrum of MND-Ox presents a prominent band at 1796 cm^{-1} corresponding to C=O stretching vibrations of carboxylic acids and anhydrides. The broad band from 1000 to 1250 cm^{-1} with a maximum at 1108 cm^{-1} corresponds to C-O stretching involved in hydroxyl and ether groups and confirms that MND-Ox present an oxidized surface chemistry. For MND-H, the effective hydrogenation can be assessed by the presence of C-H stretching bands at 2922 and 2852 cm^{-1}, associated with hydrogen terminations on (100) and (110) facets[24]. A shoulder is also noticeable at 2830 cm^{-1} corresponding to (111) facets. Only for MND-H, a dip in the absorbance is visible at 1330 cm^{-1}. This particularity is the focus of recent studies, attributing this phenomenon to a surface conductivity of MND-H in water[15,25–27]. Note that for both MND-H and MND-Ox samples, bands located at *ca*. 3300 cm^{-1} and 1620 cm^{-1} associated respectively to O–H

stretching and bending modes may be partially or totally related to the presence of water molecules since infrared measurements were performed under air at ambient temperature.

To obtain information on the colloidal behavior and stability of these suspensions, DLS and ZP measurements were realized (Figure 2b). For MNDs particles, the average hydrodynamic diameter was around 30 nm whatever the surface chemistry. Meanwhile, their zeta potentials were good indicators of the success of the different treatments, with opposite charges detected, ranging from – 67 mV for MND-Ox to + 47 mV for MND-H, in agreement with the literature[28].

We then evaluated the impact of annealings on the atomic composition and carbon binding states through XPS analysis of MNDs suspensions (Table 1).

Atomic %	**MND-Ox**	**MND-H**
Carbon	91.5	98.5
Oxygen	8.5	1.5
Nitrogen	ND	ND
% of the C_{1s} area		
sp^3-C	61	82.5
sp^2-C	7	3
Defects	17.5	8
C-O-C	7.5	5
C=O	7	1.5

Table 1 : Atomic percentages of carbon, oxygen and nitrogen in MND-Ox and MND-H and results of the C_{1s} core fit of each sample. ND = Not Detected. Estimated error on values is *ca.* 2.5%.

For each sample, carbon is, as expected, the predominant component of MNDs with atomic percentages higher than 91 %, followed by oxygen. MND-Ox particles have the highest oxygen atomic percentage (8.5 %) corroborating the oxidized functions detected by infrared analysis. This percentage drops to 1.5 % when these particles are hydrogenated. It is noticeable that nitrogen is below the XPS detection limit (< 0.5 at %[29]) which is usually not the case for DNDs due to their synthesis precursors[30].

To investigate the types of carbon bonding present in these MNDs, deconvolution of the C_{1s} core levels of each spectrum was realized using previously described methodology[15] (Figure S2). For both samples, the vast majority of carbon atoms are of sp^3 configuration, which reflects the high quality of the crystalline diamond core in HPHT synthesized diamond. This percentage is slightly higher for MND-H than for MND-Ox. The contribution of sp^2-carbon was estimated at 7 % of the C_{1s} area for MND-Ox particles, and drops to 3 % after hydrogenation, suggesting an etching of sp^2-C by the H_2 treatment. "Defects" in Table 1 refers to carbon atoms not directly bonded to oxygen, including sp^3-C close to structural defects. For MNDs particles, the content of defects is quite low, 17.5 % for MND-Ox and 8 % for MND-H, which is in line with the long-range order of sp^3 carbon in diamond crystalline lattice. Finally, at the highest binding energies of the C_{1s} core, carbon linked to oxygen atoms can be found, simply (C-O-C) and doubly linked (C=O). These percentages are higher for oxidized MNDs than for hydrogenated ones, as expected. This XPS analysis confirms the preservation of sp^3-C and the modification of the atomic composition of MND-H and MND-Ox after surface treatments.

According to these complementary techniques, not only the effective oxidation and hydrogenation of MNDs were confirmed, but also the colloidal stability of each suspension, making them suitable for further irradiation experiments.

Quantification of solvated electrons

Our concern in this study was to evaluate the impact of MNDs on the formation of solvated electrons and hydroxyl radicals during γ-radiolysis. As these radical species have very short lifetimes, probes were needed for their quantification. For e^-_{solv} quantification, the indirect detection we implemented was based on the reduction of nitrate ions by solvated electrons, leading to the formation of nitrite ions[31,32] (Eq. 2).

$$NO_3^- + 2\,e^-_{solv} + 2\,H^+ \rightarrow NO_2^- + H_2O \quad (2)$$

The first step of this reaction is the monoelectronic reduction of NO_3^- into $NO_3^{\bullet 2-}$ that occurs with a rate constant[33] of 9.7 x 10^9 L.mol^{-1}.s^{-1}. Therefore, a 2 mM initial concentration of nitrate ions corresponds to a reaction time with solvated electrons of *ca*. 52 ns. The diazotation reaction between nitrite ions and 2,3-diaminonaphthalene (2,3-DAN) produces 2,3-naphtotriazole (2,3-NAT), whose fluorescence signal is linear over a large range of nitrite concentrations, allowing the indirect quantification of electrons over a large dose range. The protocol was adapted and optimized from previous works[34–36], resulting in a simple process, compatible with samples containing nanoparticles[37]. The slope of the fit always presented a linear evolution, as can be seen in Figure 3a, and represents the formation yield of NO_2^-, or G-value, usually expressed in mol.J^{-1}. We plotted in Figure 3b the ratio of the G-values for nitrite ions with and without MND-H and MND-Ox, allowing an easier comparison with water radiolysis.

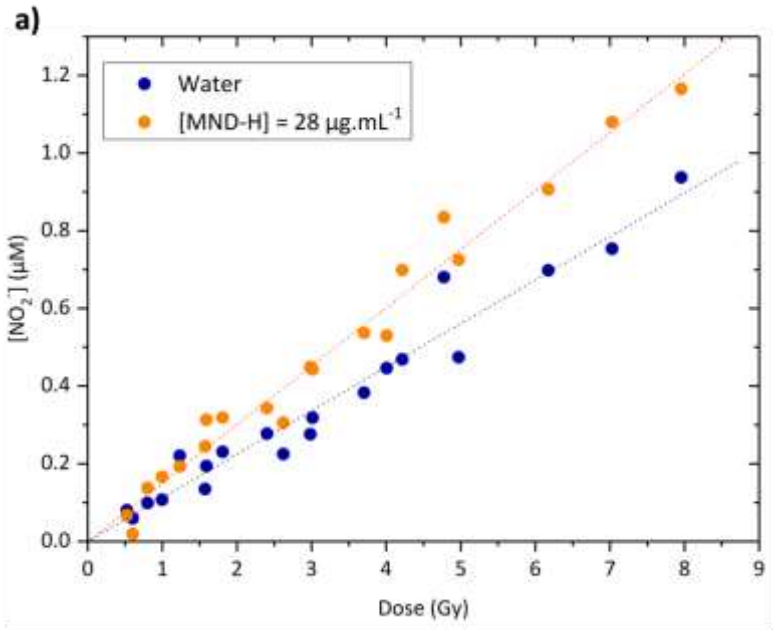

Figure 3: a) Evolution of NO_2^- concentration as a function of the dose for water and MND-H (28 µg/mL). b) Ratio of the formation yields of nitrite ions in solution under irradiation as a function of MNDs concentration for both surface chemistries. The dotted line represents the values when only water is irradiated.

The apparent formation yield of nitrite ions increases with MND-H concentration till approximately 10 $\mu g.mL^{-1}$ where a plateau begins, attributed to competition reactions. Such a trend was already observed for DND-H particles[14]. This progression is linear for the lowest concentrations, with a 30% increase in nitrite ions for 5 $\mu g.mL^{-1}$, reflecting a corresponding increase in solvated electrons production. To our best knowledge, this is the first experimental evidence of an increase in solvated electrons, available for subsequent reductions, when hydrogenated MNDs aqueous suspensions are irradiated by high-energy photons. For MND-Ox, a moderate increase of $G(NO_2^-)$ was also observed. For concentrations below 5 $\mu g.mL^{-1}$, the ratio rises quite similarly as with MND-H but it reaches its limit at *ca*. 15 % of the value for water within the explored concentration range (4-30 $\mu g.mL^{-1}$ max).

Quantification of hydroxyl radicals

To study the reactivity of MND particles towards hydroxyl radicals, the coumarin probe was used. It reacts with $HO^{\bullet}$ with a constant rate[38] of 1.05×10^{10} $L.mol^{-1}.s^{-1}$ to give several hydroxylation products, among which 7-hydroxycoumarin (7-OHCou) is fluorescent. Before deploying this protocol, a preliminary experiment consisting in checking if the particles modify the regioselectivity of coumarin hydroxylation was required[39]. Figure S4 presents HPLC separation of the oxidation products in irradiated samples containing coumarin only, or in the presence of MND-H or MND-Ox for similar doses. The HPLC profiles are very similar as the same hydroxycoumarins are detected in all three conditions with the same relative proportions, meaning that regioselectivity is not impacted significantly by the presence of MNDs. 7-OHCou is thus representative of all hydroxylation reactions, and so of hydroxyl radicals. Concentrations and G-values of 7-OHCou were then quantified from fluorescence measurements after irradiation.

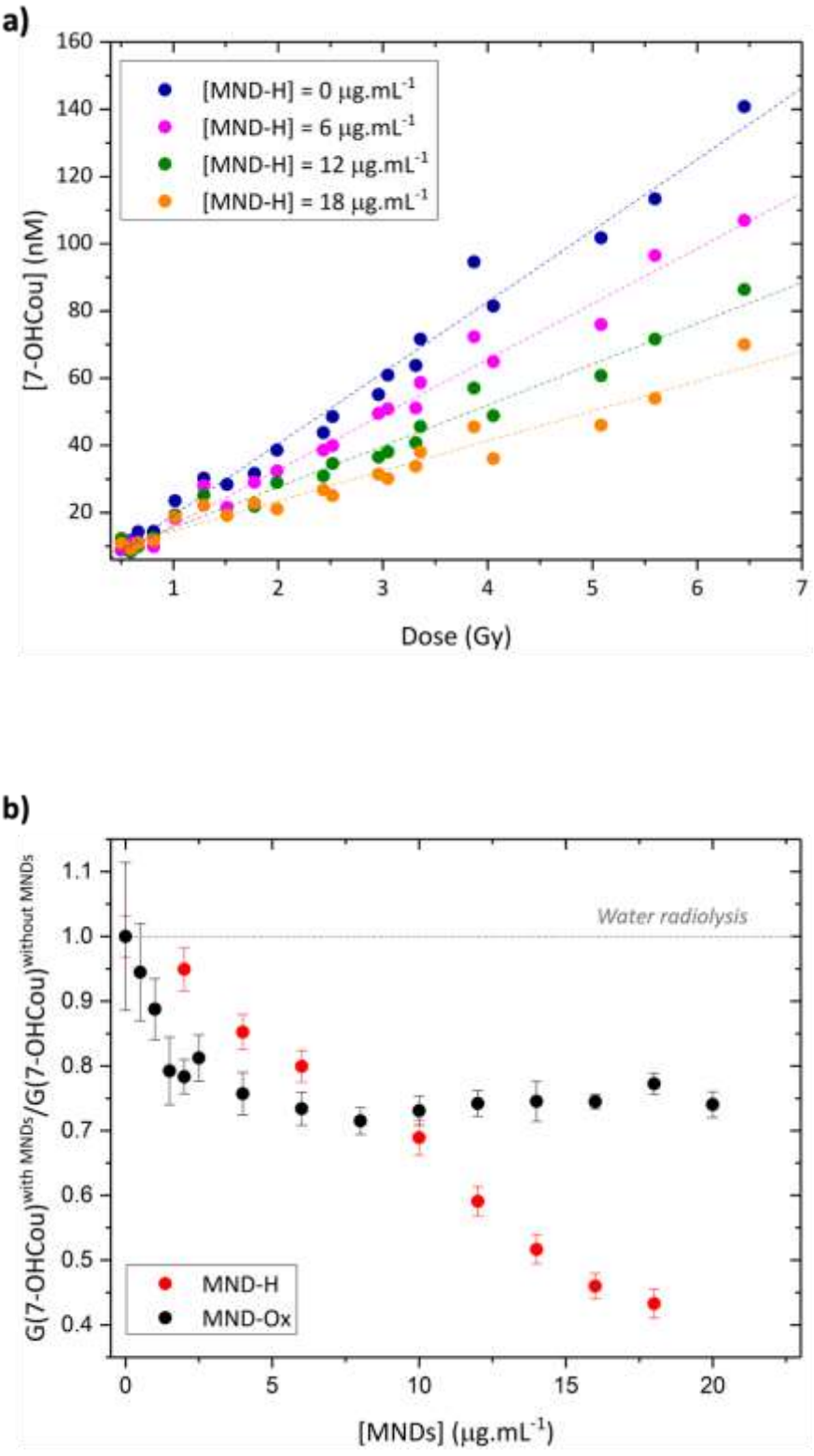

Figure 4 : a) Evolution of 7-OHCou concentration as a function of the dose for several MND-H concentrations. b) Evolution of the apparent formation yields of 7-OHCou in presence of MND-H and MND-Ox compared to water alone. Initial coumarin concentration: 0.5 mM

Figure 4a presents the evolution of the concentration of 7-OHCou as a function of the dose for different MND-H concentrations. For each condition, the concentration of 7-OHCou increases linearly with the dose, but when calculating the 7-hydroxycoumarin formation yield a decrease is obtained with increasing MND-H concentration. This means that fewer $HO^{\bullet}$ radicals are scavenged by coumarin in solution in the presence of nanoparticles than for water alone. While a 7-OHCou apparent formation yield of 21 $nmol.J^{-1}$ was found without MNDs, this value went down whatever the concentration of MND-H particles. In Figure 4b, the ratio of G-values of 7-OHCou with or without MNDs is plotted. For MND-H, the decrease seems linear with the massic concentration of particles whereas MND-Ox particles present a different evolution of the formation yield of 7-OHCou. Up to 2.5 $\mu g.mL^{-1}$, a decrease of the G(7-OHCou) is observed, which is more pronounced than for MND-H. Then, it remains unchanged till the highest tested concentration of 20 $\mu g.mL^{-1}$.

Possible kinetic competitions are thus to be considered. That is why we performed similar irradiation experiments, using another MND-H aqueous suspension, varying coumarin concentration between 0.2 and 1.5 mM. Indeed, given the rate constant of the reaction between coumarin and hydroxyl radicals[38] ($k = 1.05 \times 10^{10}\ M^{-1}.s^{-1}$), a 0.2 mM coumarin solution reacts with $HO^{\bullet}$ in *ca.* 480 ns after the initial transfer of energy to water compared to *ca.* 60 ns for a 1.5 mM coumarin solution. Under continuous irradiation, the system can be considered in steady-state as regards $HO^{\bullet}$, therefore increasing coumarin concentration increases the fraction of $HO^{\bullet}$ reacting with it. The results of this competition for MND-H are presented in Figure 5.

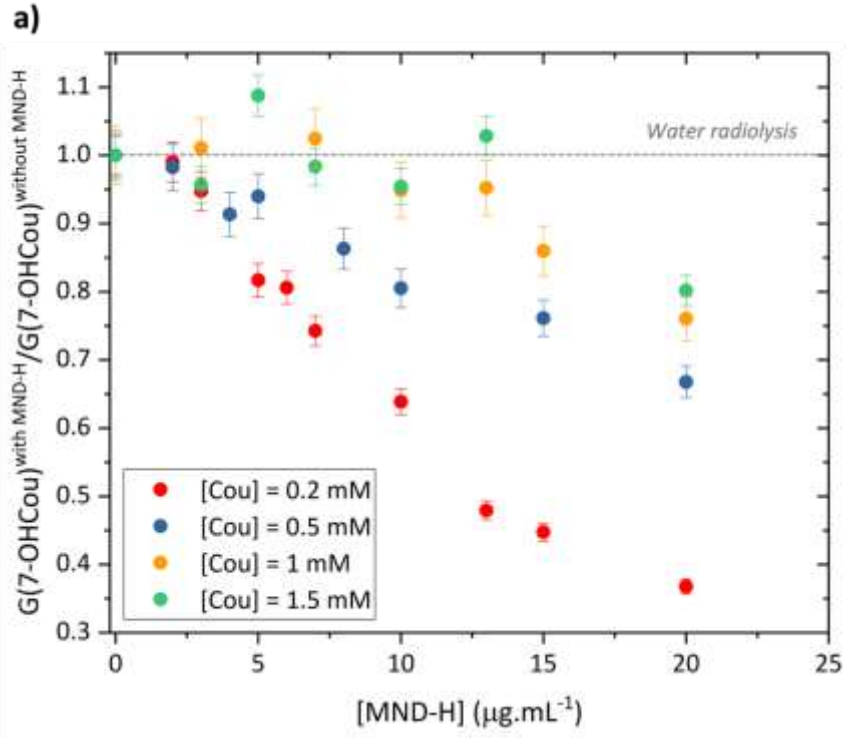
a)
Water radiolysis
[Cou] = 0.2 mM
[Cou] = 0.5 mM
[Cou] = 1 mM
[Cou] = 1.5 mM
G(7-OHCou)with MND-H/G(7-OHCou)without MND-H
[MND-H] (µg.mL-1)

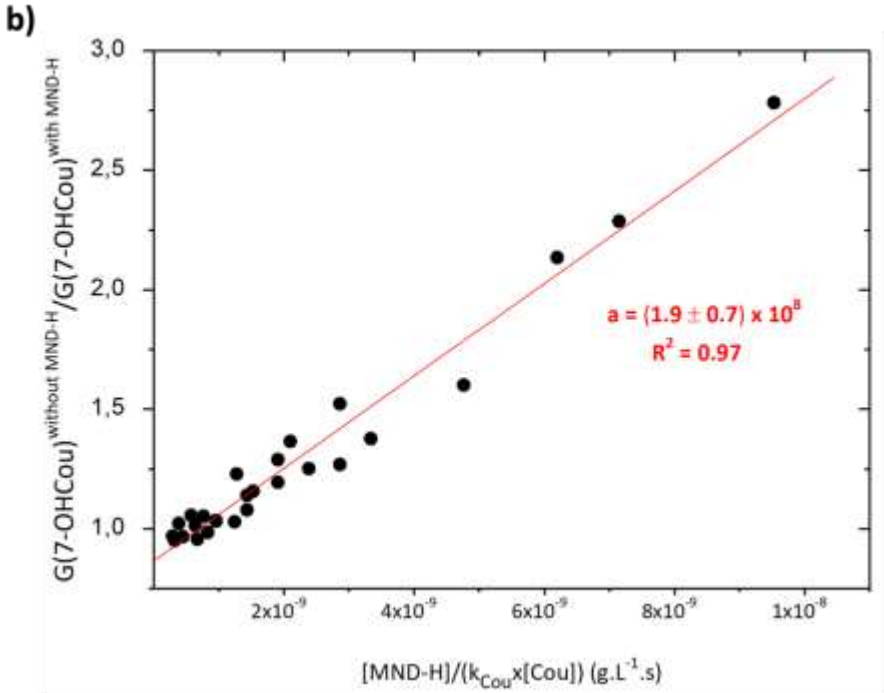
b)
a = (1.9 ± 0.7) x 10^8
R2 = 0.97
G(7-OHCou)without MND-H/G(7-OHCou)with MND-H
[MND-H]/(kCou x[Cou]) (g.L-1.s)

Figure 5: a) Evolution of the formation yield of 7-OH coumarin with MND-H concentration for different initial coumarin concentrations, b) Determination of the apparent rate constant of HO• radicals with MND-H.

Comparing the results for 0.2 and 0.5 mM concentrations, higher coumarin concentration results in a higher G-value of 7-OHCou. For 1 and 1.5 mM, a G-value equivalent to the one of water radiolysis is measured for MND-H concentrations up to 7 $\mu g.mL^{-1}$. For higher concentrations, scavenging by MNDs is again visible. This evidences a competition between coumarin and MND-H for scavenging hydroxyl radicals. It is important to note that even at the higher coumarin concentrations, the G-values are equal to or smaller than the G-value of pure water solution, revealing the absence of supplementary HO• when MND-H are irradiated. Also, these experiments allowed us to extract the rate constant for the reaction between MND-H and HO• (k_{MND-H}) using Eq. 3 adapted from previous studies[40,41]:

$$\frac{G(7-OHCou)^{without\ MND-H}}{G(7-OHCou)^{with\ MND-H}} = 1 + k_{MND-H} \times \frac{[MND-H]}{k_{cou} \times [Cou]} \quad (3)$$

The fit of the plot presented in Figure 5b gives us an estimate k_{MND-H} of $1.9 \pm 0.7.10^8$ $L.g^{-1}.s^{-1}$.

As HO• is known to react with any molecule due to its high redox potential, this scavenging could be caused by the presence of any contaminant in or at the surface of MND-H samples, reacting more rapidly with HO• than coumarin. To assess this hypothesis, NaCl salt was added to MNDs samples to increase ionic strength, resulting in MND-H precipitation and the release of weakly bound species at the particles' surface. The supernatant was then irradiated and results, presented in Figure 6, showed an identical G(7-OHCou) for coumarin alone or irradiated with the supernatant. This shows that MND-H particles by themselves present scavenging properties towards HO•.

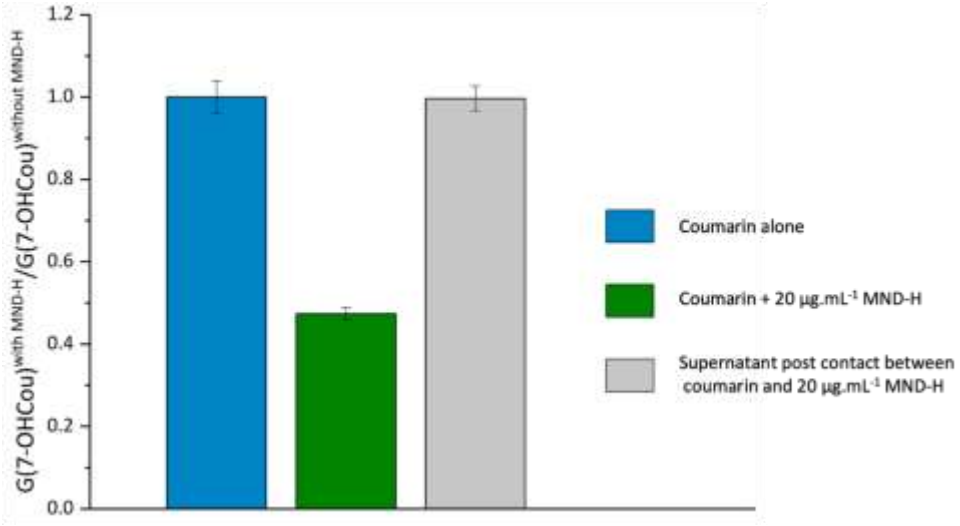

Figure 6 : Comparison of the yield of 7-OHCou production for coumarin (0.5 mM) irradiated in water, in the presence of 20 µg.mL^{-1} MND-H and with MND-H supernatant. The supernatant was obtained after incubation with 1% (w/v) final NaCl and centrifugation.

To detect any HO•-induced modification of MND-H surface, concentrated suspensions were irradiated at higher dose and analyzed by XPS and FTIR (Figure 7). The dose was chosen to keep the ratio between concentrations of radicals and particles in the same order of magnitude for this experiment and the ones with coumarin. The main observation was that colloidal stability was lost after irradiation, leading to a visible precipitate of MND-H. XPS analysis revealed that the oxygen atomic percentage went from 1.5 to 2.5 at % after irradiation.

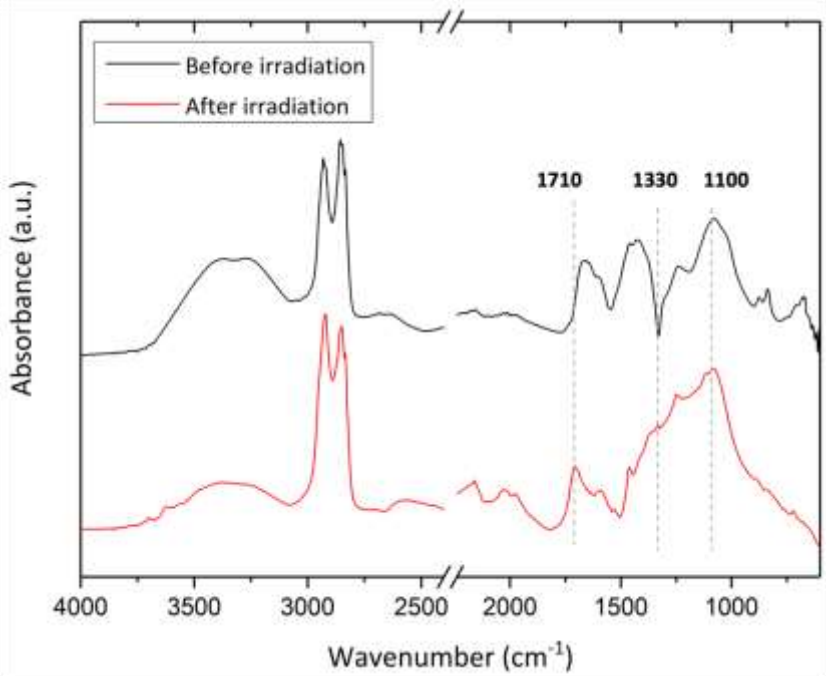

Figure 7 : FTIR spectra of MND-H suspensions before (top, black) and after (bottom, red) irradiation. A concentrated suspension of MND-H (5.6 mg.mL^{-1}) was irradiated at 1200 Gy.

As can be seen in Figure 7, irradiation also induces modifications in the MND-H infrared spectra. Signatures of C-H bonds are still present but a new band is visible at 1710 cm^{-1}, usually associated with C=O bonds of ketones and aldehydes. Also, the C-O stretching modes at 1100-1200 cm^{-1} seem more prominent. These analyses confirm that the irradiation induced an oxidation of MND-H surface. Besides, one can notice that the dip in the absorbance at 1330 cm^{-1} is lost after irradiation. It is in agreement with previous observations where this optical phenomenon is only present for MND-H stable in suspension[15].

Discussion

Recently, optimal hydrogenation conditions to obtain stable suspensions of MND-H in water over months were reported[15,42], which opens the way for new investigations as presented in this paper.

With stable suspensions, we were able to study how MNDs behave under gamma irradiation through the quantification of hydroxyl radicals and solvated electrons available in solution.

We focused on MND-H particles as a hydrogenated surface is required for negative electron affinity (NEA), enabling a facilitated electron emission when electrons are excited into the conduction band[43]. A set of complementary techniques documented that H_2-annealing led to the reduction of oxygenated functions, etching of non-diamond phase, and creation of C-H bonds on the different facets. Submitted to high-energy photons, MND-H increased the available quantity of solvated electrons but not of hydroxyl radicals. On the opposite, they scavenged hydroxyl radicals very efficiently. These results could be compared with previous studies realized with DNDs[14]. Under gamma irradiation, colloids of hydrogenated DNDs exhibit an equal overproduction of hydroxyl radicals and solvated electrons while in the case of MNDs, for similar coumarin concentrations, no overproduction of $HO^{\bullet}$ radicals was detected. We previously proposed, as for other nanomaterials[44], that interfacial water could play an essential role in radicals' production in solution when DND-H were irradiated[14]. This hypothesis is supported by experimental data revealing different structures of water molecules surrounding detonation nanodiamonds when the surface chemistry is varied[45] and simulation results on gold nanoparticles[46]. The possible weakening of O-H bonds in water molecules near the DND-H surface could locally amplify water radiolysis, leading to hydroxyl radicals and solvated electrons in the same proportions. Obviously, mechanisms for milled nanodiamonds are different as only electrons seem to be overproduced.

As solvated electrons are among the most reductive species in aqueous environment, they arouse lively interest. In previous studies, we used to quantify solvated electrons available in solution under deaerated atmosphere, a method based on the transformation of electrons into hydroxyl radicals by N_2O, and subsequent detection by coumarin[39]. In this work, samples were irradiated

under air, and electrons were quantified based on the reduction of nitrate into nitrite ions, detected by 2,3-DAN. On the one hand, this protocol presents the main advantage that samples do not need to be degassed before irradiation; on the other hand, as a preliminary step, colloidal stability must be studied as a function of nitrate ions concentration to determine working concentration. 2 mM was chosen as it preserves colloidal suspensions and allows to capture electrons twice more rapidly than dissolved dioxygen. Indeed, electron scavenging is favored by higher nitrate concentration but as ionic strength increases, it can cause flocculation and sedimentation of particles. For a concentration as low as 20 $\mu g.mL^{-1}$, MND-H led to 45 % supplementary electrons in solution compared to water, while DND-H at the same massic concentration led to 50%, which is of the same order of magnitude. Saoudi *et al*. proposed that such MND-H must behave like bulk diamond as they observed the shift of their valence and conductive bands[15]. Their NEA would facilitate electron transfer from the particle onto the solution if their electrons are excited with energies higher than 5.5 eV, which is the bandgap of diamond. In our case, MeV photons, as well as Cerenkov light, have enough energy to trigger this phenomenon. Regarding the absence of coumarin hydroxylation, either these emitted electrons are not energetic enough to cause secondary radiolysis, or secondary radiolysis occurs very locally at the surface of MND, the resulting $HO^{\bullet}$ being then scavenged by the diamond surface. As demonstrated by numerous complementary characterizations, MNDs are different from DNDs in many points such as crystalline quality, large crystallographic facets, polydispersity or surface chemistry and they present different behaviors under irradiation. Further investigations are needed to assign to these different features a role, if any, in the mechanisms of radical production.

Another striking fact for MND-H suspensions is the loss of colloidal stability following irradiation. FTIR spectra and XPS analysis confirmed the oxidation of the irradiated MND-H as well as the induced loss of the surface conductivity, the latter being probed by the dip of absorbance

which is peculiar to stable colloids. Co-existence of C-H terminations, that confer positive zeta potential, with irradiation-induced oxygenated groups could result in a modified zeta potential, and eventually flocculation of the samples. This is also in agreement with the study from Zhang and Hamers who demonstrated that H-terminated MNDs, in the absence of an electron donor, show clear signs of oxidation and aggregation under illumination[12]. So destabilization seems also to occur for hydrogenated particles of high crystallinity of smaller sizes.

Surprisingly, MND-H do not present any overproduction of hydroxyl radicals as DND-H did, but scavenging properties. The main reactions of hydroxyl radicals are additions and hydrogen abstraction[47,48]. Given the C-H bonds at the MND-H surface, hydroxyl radicals can abstract some surface hydrogen atoms, to form water molecules, generating carbon-centered radicals. The latter can react with dissolved oxygen or water molecules to form oxidized functions, which is supported by the infrared and XPS analyses after irradiation. $HO^{\bullet}$ can also add on remaining C=C bonds though sp^2-C content on MND-H is only 2 % of the whole carbon content. Varying coumarin concentration, we obtained an estimated rate constant of MND-H with hydroxyl radicals of $k_{MND\text{-}H} = 1.9 \pm 0.7 \times 10^8$ $L.g^{-1}.s^{-1}$. Because of the polydispersity of MNDs, it is unreliable to convert massic into molar concentrations to obtain a value comparable to those available for other antioxidant species. Nevertheless, Que *et al*. recently applied the same methodology to investigate the antioxidant properties of MXenes, which are nanosheets containing carbon and nitrogen atoms as well as early transition metals[49]. They found a rate constant of 1.58×10^8 $L.g^{-1}.s^{-1}$ which means that both material rate constants are in the same order of magnitude. It is also possible to convert the mass concentration into the solid surface area to solution volume ratio as in Li *et al.*[41], which gives $k_{MND\text{-}H} = 1120 \pm 400$ $m.s^{-1}$, a 50-fold higher value than the one reported for carbon black. For MND-Ox, the reactivity is different. As confirmed with HPLC analyses, this behavior is not due to different coumarin hydroxylation patterns. It can be noticed that these oxidized particles

present three times more sp^2-carbon than MND-H, according to the XPS analysis. Some rare hydrogen terminations might also subsist at MND-Ox surface, even if not visible by FTIR. But overall there are fewer attack sites on MND-Ox than MND-H, which could explain why they are less efficient to scavenge $HO^{\bullet}$ (for concentrations above 10 $\mu g.mL^{-1}$).

Also, a limited enhancement of the available quantity of solvated electrons is noticed for MND-Ox. This differs from what was observed for DND-Ox for which we previously reported no overproduction of solvated electrons[14]. Recent literature reports also this observation for UV illumination of HPHT synthetized NDs with an oxidized chemistry[13]. As mentioned before, while hydrogenated surface chemistry would induce an overproduction of electrons, photons from gamma irradiation have enough energy to trigger the emission from an oxidized surface. Given these observations, the question of using MNDs as antioxidants and electron emitters is open. Since the scavenging of hydroxyl radicals leads to an oxidation of the MNDs surface, a decrease in the scavenging and overproducing efficiencies might happen. Given the strong interest in photocatalysis perspectives of HPHT synthetized nanodiamonds, a main challenge could be then to prevent MNDs surface oxidation while maintaining electron emission. The addition of sacrificial donors, as it was proposed elsewhere[12], could be a wise approach.

Conclusion

The radical species reactivities towards nanodiamonds are crucial for considering applications in radiomedicine or (photo)catalysis. In the present study, we brought new insights on milled nanodiamonds (MNDs) behavior under irradiation by revealing opposite reactivities of MNDs towards hydroxyl radicals and solvated electrons. Using nanoparticle-compatible and optimized methods, we put into light that the irradiation of MNDs aqueous suspensions with MeV photons leads to an overproduction of solvated electrons, more pronounced for hydrogenated than oxidized

MNDs. In contrast, for the first time, we evidenced a $HO^{\bullet}$ scavenging behavior of MNDs whose intensity is also surface chemistry dependent. Our results suggest that MND particles, especially hydrogenated, can be considered either as photocatalysts or as antioxidant agents.

ASSOCIATED CONTENT

Supporting information

Supporting information consists of cryo-EM observation of untreated MNDs, N_2 adsorption isotherm of MND-AsR, MND-Ox and MND-H powders, XPS C_{1s} spectra and deconvolutions of MND-Ox and MND-H, HPLC profiles of irradiated coumarin (0.5 mM) solutions alone and in the presence of 20 $\mu g.mL^{-1}$ MND-H or MND-Ox.

AUTHOR INFORMATION

Corresponding Author

Cécile Sicard-Roselli - Institut de Chimie Physique, UMR 8000, CNRS, Université Paris-Saclay, 91405 Orsay, France

cecile.sicard@universite-paris-saclay.fr

Authors

Florent Ducrozet - Institut de Chimie Physique, UMR 8000, CNRS, Université Paris-Saclay, 91405 Orsay, France ; Université Paris-Saclay, CEA, CNRS, NIMBE, 91191 Gif sur Yvette, France

Emilie Brun - Institut de Chimie Physique, UMR 8000, CNRS, Université Paris-Saclay, 91405 Orsay, France

Hugues A. Girard - Université Paris-Saclay, CEA, CNRS, NIMBE, 91191 Gif sur Yvette, France

Jean-Charles Arnault - Université Paris-Saclay, CEA, CNRS, NIMBE, 91191 Gif sur Yvette, France

Authors Contributions

All authors participated in the investigation, analysis and writing draft.

ACKNOWLEDGMENTS

The authors would like to thank Charles Rivron and Jocelyne Leroy from CEA NIMBE for N_2 adsorption experiments and XPS analysis and Eric Larquet from PMC Lab (Ecole Polytechnique, CNRS) for cryo-EM observations.

REFERENCES

(1) Wang, H.; Cui, Y. Nanodiamonds for Energy. *Carbon Energy* **2019**, *1* (1), 13–18. https://doi.org/10.1002/cey2.9.

(2) Kidalov, S. V.; Shakhov, F. M.; Vul, A. Ya. Thermal Conductivity of Sintered Nanodiamonds and Microdiamonds. *Diam. Relat. Mater.* **2008**, *17* (4–5), 844–847. https://doi.org/10.1016/j.diamond.2008.01.091.

(3) Piña-Salazar, E.-Z.; Sagisaka, K.; Hattori, Y.; Sakai, T.; Futamura, R.; Ōsawa, E.; Kaneko, K. Electrical Conductivity Changes of Water-Adsorbed Nanodiamonds with Thermal Treatment. *Chem. Phys. Lett.* **2019**, *737*, 100018. https://doi.org/10.1016/j.cpletx.2019.100018.

(4) Mochalin, V. N.; Gogotsi, Y. Nanodiamond–Polymer Composites. *Diam. Relat. Mater.* **2015**, *58*, 161–171. https://doi.org/10.1016/j.diamond.2015.07.003.

(5) Qin, J.-X.; Yang, X.-G.; Lv, C.-F.; Li, Y.-Z.; Liu, K.-K.; Zang, J.-H.; Yang, X.; Dong, L.; Shan, C.-X. Nanodiamonds: Synthesis, Properties, and Applications in Nanomedicine. *Mater. Des.* **2021**, *210*, 110091. https://doi.org/10.1016/j.matdes.2021.110091.

(6) Amaral, M.; Dias, A. G.; Gomes, P. S.; Lopes, M. A.; Silva, R. F.; Santos, J. D.; Fernandes, M. H. Nanocrystalline Diamond: In Vitro Biocompatibility Assessment by MG63 and Human Bone Marrow Cells Cultures. *J. Biomed. Mater. Res. A* **2008**, *87A* (1), 91–99. https://doi.org/10.1002/jbm.a.31742.

(7) El-Eskandarany, M. S.; Al-Hazza, A.; Al-Hajji, L. A.; Ali, N.; Al-Duweesh, A. A.; Banyan, M.; Al-Ajmi, F. Mechanical Milling: A Superior Nanotechnological Tool for Fabrication of Nanocrystalline and Nanocomposite Materials. *Nanomaterials* **2021**, *11* (10), 2484. https://doi.org/10.3390/nano11102484.

(8) Stehlik, S.; Mermoux, M.; Schummer, B.; Vanek, O.; Kolarova, K.; Stenclova, P.; Vlk, A.; Ledinsky, M.; Pfeifer, R.; Romanyuk, O.; et al. Size Effects on Surface Chemistry and Raman Spectra of Sub-5 Nm Oxidized High-Pressure High-Temperature and Detonation Nanodiamonds. *J. Phys. Chem. C* **2021**, *125* (10), 5647–5669. https://doi.org/10.1021/acs.jpcc.0c09190.

(9) Van Der Laan, KiranJ.; Hasani, M.; Zheng, T.; Schirhagl, R. Nanodiamonds for In Vivo Applications. *Small* **2018**, *14* (19), 1703838. https://doi.org/10.1002/smll.201703838.

(10) Segawa, T. F.; Igarashi, R. Nanoscale Quantum Sensing with Nitrogen-Vacancy Centers in Nanodiamonds – A Magnetic Resonance Perspective. *Prog. Nucl. Magn. Reson. Spectrosc.* **2023**, *134–135*, 20–38. https://doi.org/10.1016/j.pnmrs.2022.12.001.

(11) Ajoy, A.; Safvati, B.; Nazaryan, R.; Oon, J. T.; Han, B.; Raghavan, P.; Nirodi, R.; Aguilar, A.; Liu, K.; Cai, X.; et al. Hyperpolarized Relaxometry Based Nuclear T1 Noise Spectroscopy in Diamond. *Nat. Commun.* **2019**, *10* (1), 5160. https://doi.org/10.1038/s41467-019-13042-3.

(12) Zhang, L.; Hamers, R. J. Photocatalytic Reduction of CO2 to CO by Diamond Nanoparticles. *Diam. Relat. Mater.* **2017**, *78* (April), 24–30. https://doi.org/10.1016/j.diamond.2017.07.005.

(13) Buchner, F.; Kirschbaum, T.; Venerosy, A.; Girard, H.; Arnault, J.-C.; Kiendl, B.; Krueger, A.; Larsson, K.; Bande, A.; Petit, T.; Merschjann, C. Early Dynamics of the Emission of Solvated Electrons from Nanodiamonds in Water. *Nanoscale* **2022**, *14* (46), 17188–17195. https://doi.org/10.1039/D2NR03919B.

(14) Brun, E.; Girard, H. A.; Arnault, J.-C.; Mermoux, M.; Sicard-Roselli, C. Hydrogen Plasma Treated Nanodiamonds Lead to an Overproduction of Hydroxyl Radicals and Solvated Electrons in Solution under Ionizing Radiation. *Carbon* **2020**, *162*, 510–518. https://doi.org/10.1016/j.carbon.2020.02.063.

(15) Saoudi, L.; Girard, H. A.; Larquet, E.; Mermoux, M.; Leroy, J.; Arnault, J.-C. Colloidal Stability over Months of Highly Crystalline High-Pressure High-Temperature Hydrogenated Nanodiamonds in Water. *Carbon* **2023**, *202* (P1), 438–449. https://doi.org/10.1016/j.carbon.2022.10.084.

(16) Fricke, H.; Morse, S. XIII. The Action of X-Rays on Ferrous Sulphate Solutions. *Lond. Edinb. Dublin Philos. Mag. J. Sci.* **1929**, *7* (41), 129–141. https://doi.org/10.1080/14786440108564721.

(17) Gopakumar, K.; Kini, U. R.; Ashawa, S. C.; Bhandari, N. S.; Krishnan, G. U.; Krishnan, D. Gamma Irradiation of Coumarin in Aqueous Solution. *Radiat. Eff.* **1977**, *32* (3–4), 199–203. https://doi.org/10.1080/00337577708233075.

(18) Leandri, V.; Gardner, J. M.; Jonsson, M. Coumarin as a Quantitative Probe for Hydroxyl Radical Formation in Heterogeneous Photocatalysis. *J. Phys. Chem. C* **2019**, *123* (11), 6667–6674. https://doi.org/10.1021/acs.jpcc.9b00337.

(19) Krueger, A. Current Issues and Challenges in Surface Chemistry of Nanodiamonds. In *Nanodiamonds*; Elsevier, 2017; pp 183–242. https://doi.org/10.1016/B978-0-32-343029-6.00008-8.

(20) Xu, N. S.; Chen, J.; Deng, S. Z. Effect of Heat Treatment on the Properties of Nano-

Diamond under Oxygen and Argon Ambient. *Diam. Relat. Mater.* **2002**, *11* (2), 249–256. https://doi.org/10.1016/S0925-9635(01)00680-X.

(21) Sing, K. S. W. Reporting Physisorption Data for Gas/Solid Systems with Special Reference to the Determination of Surface Area and Porosity (Recommendations 1984). *Pure Appl. Chem.* **1985**, *57* (4), 603–619. https://doi.org/10.1351/pac198557040603.

(22) Costa, G. C. C.; Shenderova, O.; Mochalin, V.; Gogotsi, Y.; Navrotsky, A. Thermochemistry of Nanodiamond Terminated by Oxygen Containing Functional Groups. *Carbon* **2014**, *80*, 544–550. https://doi.org/10.1016/j.carbon.2014.08.094.

(23) Petit, T.; Puskar, L. FTIR Spectroscopy of Nanodiamonds: Methods and Interpretation. *Diam. Relat. Mater.* **2018**, *89* (December 2017), 52–66. https://doi.org/10.1016/j.diamond.2018.08.005.

(24) Cheng, C. L.; Chen, C. F.; Shaio, W. C.; Tsai, D. S.; Chen, K. H. The CH Stretching Features on Diamonds of Different Origins. *Diam. Relat. Mater.* **2005**, *14* (9), 1455–1462. https://doi.org/10.1016/j.diamond.2005.03.003.

(25) Kudryavtsev, O. S.; Bagramov, R. H.; Satanin, A. M.; Shiryaev, A. A.; Lebedev, O. I.; Romshin, A. M.; Pasternak, D. G.; Nikolaev, A. V.; Filonenko, V. P.; Vlasov, I. I. Fano-Type Effect in Hydrogen-Terminated Pure Nanodiamond. *Nano Lett.* **2022**, *22* (7), 2589–2594. https://doi.org/10.1021/acs.nanolett.1c04887.

(26) Shiryaev, A. A.; Ekimov, E.; Prokof'ev, V. Y.; Kondrin, M. Temperature Dependence of Fano Resonance in Nanodiamonds Synthesized at High Static Pressures. *JETP Lett.* **2022**. https://doi.org/10.31857/S1234567822110039.

(27) Ekimov, E.; Shiryaev, A. A.; Grigoriev, Y.; Averin, A.; Shagieva, E.; Stehlik, S.; Kondrin, M. Size-Dependent Thermal Stability and Optical Properties of Ultra-Small Nanodiamonds Synthesized under High Pressure. *Nanomaterials* **2022**, *12* (3), 351. https://doi.org/10.3390/nano12030351.

(28) Arnault, J.-C. Surface Modifications of Nanodiamonds and Current Issues for Their Biomedical Applications. In *Novel Aspects of Diamond - From Growth to Applications*; 2015; pp 85–122. https://doi.org/10.1007/978-3-319-09834-0_4.

(29) Arnault, J. C. X-Ray Photoemission Spectroscopy Applied to Nanodiamonds: From Surface Chemistry to in Situ Reactivity. *Diam. Relat. Mater.* **2018**, *84* (November 2017), 157–168. https://doi.org/10.1016/j.diamond.2018.03.015.

(30) Dolmatov, V. Y.; Ozerin, A. N.; Kulakova, I. I.; Bochechka, O. O.; Lapchuk, N. M.; Myllymäki, V.; Vehanen, A. Detonation Nanodiamonds: New Aspects in the Theory and Practice of Synthesis, Properties and Applications. *Russ. Chem. Rev.* **2020**, *89* (12), 1428–1462. https://doi.org/10.1070/RCR4924.

(31) Horne, G. P.; Donoclift, T. A.; Sims, H. E.; Orr, R. M.; Pimblott, S. M. Multi-Scale Modeling of the Gamma Radiolysis of Nitrate Solutions. *J. Phys. Chem. B* **2016**, *120* (45), 11781–11789. https://doi.org/10.1021/acs.jpcb.6b06862.

(32) Yakabuskie, P. A.; Joseph, J. M.; Stuart, C. R.; Wren, J. C. Long-Term γ-Radiolysis Kinetics of NO 3 − and NO 2 − Solutions. *J. Phys. Chem. A* **2011**, *115* (17), 4270–4278.

https://doi.org/10.1021/jp200262c.

(33) Buxton, G. V.; Greenstock, C. L.; Helman, W. P.; Ross, A. B. Critical Review of Rate Constants for Reactions of Hydrated Electrons, Hydrogen Atoms and Hydroxyl Radicals (·OH/·O − in Aqueous Solution. *J. Phys. Chem. Ref. Data* **1988**, *17* (2), 513–886. https://doi.org/10.1063/1.555805.

(34) Carré, M.-C.; Mahieuxe, B.; André, J.-C.; Viriot, M.-L. Fluorimetric Nitrite Analysis Using 2,3-Diaminonaphthalene: An Improvement of the Method. *Analusis* **1999**, *27* (10), 835–838. https://doi.org/10.1051/analusis:1999101.

(35) Misko, T. P.; Schilling, R. J.; Salvemini, D.; Moore, W. M.; Currie, M. G. A Fluorometric Assay for the Measurement of Nitrite in Biological Samples. *Anal. Biochem.* **1993**, *214* (1), 11–16. https://doi.org/10.1006/abio.1993.1449.

(36) Damiani, P.; Burini, G. Fluorometric Determination of Nitrite. *Talanta* **1986**, *33* (8), 649–652. https://doi.org/10.1016/0039-9140(86)80151-5.

(37) Ducrozet, F.; Girard, H. A.; Jianu, T.; Peulon, S.; Brun, E.; Sicard-Roselli, C.; Arnault, J.-C. Unintentional Formation of Nitrate and Nitrite Ions during Nanodiamonds Sonication: A Source of Radical and Electron Scavengers. *Colloids Surf. Physicochem. Eng. Asp.* **2023**, *663*, 131087. https://doi.org/10.1016/j.colsurfa.2023.131087.

(38) Louit, G.; Foley, S.; Cabillic, J.; Coffigny, H.; Taran, F.; Valleix, A.; Renault, J.-P.; Pin, S. The Reaction of Coumarin with the OH Radical Revisited: Hydroxylation Product Analysis Determined by Fluorescence and Chromatography. *Radiat. Phys. Chem.* **2005**, *72* (2–3), 119–124. https://doi.org/10.1016/j.radphyschem.2004.09.007.

(39) Gilles, M.; Brun, E.; Sicard-Roselli, C. Quantification of Hydroxyl Radicals and Solvated Electrons Produced by Irradiated Gold Nanoparticles Suggests a Crucial Role of Interfacial Water. *J. Colloid Interface Sci.* **2018**, *525*, 31–38. https://doi.org/10.1016/j.jcis.2018.04.017.

(40) Louit, G.; Hanedanian, M.; Taran, F.; Coffigny, H.; Renault, J.-P.; Pin, S. Determination of Hydroxyl Rate Constants by a High-Throughput Fluorimetric Assay: Towards a Unified Reactivity Scale for Antioxidants. *The Analyst* **2009**, *134* (2), 250–255. https://doi.org/10.1039/B813871K.

(41) Li, Z.; Jonsson, M. On the Reactivity of Aqueous Radiolysis Products towards Carbon Black Used in In-Situ Radiation-Synthesis of Catalytic Nanoparticles in Graphite Electrodes. *Carbon* **2021**, *173*, 61–68. https://doi.org/10.1016/j.carbon.2020.10.094.

(42) Kolarova, K.; Bydzovska, I.; Romanyuk, O.; Shagieva, E.; Ukraintsev, E.; Kromka, A.; Rezek, B.; Stehlik, S. Hydrogenation of HPHT Nanodiamonds and Their Nanoscale Interaction with Chitosan. *Diam. Relat. Mater.* **2023**, *134*, 109754. https://doi.org/10.1016/j.diamond.2023.109754.

(43) Bolker, A.; Saguy, C.; Kalish, R. Transfer Doping of Single Isolated Nanodiamonds, Studied by Scanning Probe Microscopy Techniques. *Nanotechnology* **2014**, *25* (38). https://doi.org/10.1088/0957-4484/25/38/385702.

(44) Sicard-Roselli, C.; Brun, E.; Gilles, M.; Baldacchino, G.; Kelsey, C.; McQuaid, H.; Polin, C.; Wardlow, N.; Currell, F. A New Mechanism for Hydroxyl Radical Production in Irradiated

Nanoparticle Solutions. *Small* **2014**, *10* (16), 3338–3346. https://doi.org/10.1002/smll.201400110.

(45) Petit, T.; Puskar, L.; Dolenko, T.; Choudhury, S.; Ritter, E.; Burikov, S.; Laptinskiy, K.; Brzustowski, Q.; Schade, U.; Yuzawa, H.; et al. Unusual Water Hydrogen Bond Network around Hydrogenated Nanodiamonds. *J. Phys. Chem. C* **2017**, *121* (9), 5185–5194. https://doi.org/10.1021/acs.jpcc.7b00721.

(46) Tandiana, R.; Brun, E.; Sicard-Roselli, C.; Domin, D.; Van-Oanh, N.-T.; Clavaguéra, C. Probing the Structural Properties of the Water Solvation Shell around Gold Nanoparticles: A Computational Study. *J. Chem. Phys.* **2021**, *154* (4), 044706. https://doi.org/10.1063/5.0037551.

(47) von Sonntag, C. *Free-Radical-Induced DNA Damage and Its Repair : A Chemical Perspective* in Springer Verlag Berlin Heidelberg New York, Ed Dr Sabine Schreck, 2006, ISBN 3-540-26120-6

(48) Davies, M. J.; Dean, R. T. *Radical-Mediated Protein Oxidation : From Chemistry to Medecine* in Oxford, University Press, 1997. ISBN 0-19-850097-1; 1997; Vol. 74.

(49) Que, X.; Li, S.; Hu, Y.; Zhang, Z.; Sheng, L.; Lin, T.; Ma, J.; Peng, J.; Li, J.; Zhai, M. Fluorescence Spectroscopy Study on the Reaction of Hydroxyl Radicals and Hydrated Electrons in MXene Suspension. *J. Phys. Chem. C* **2022,** 126 (26), 10703-10712. https://doi.org/10.1021/acs.jpcc.2c00098.